



Article

Synthetic Tuning of Co^{II}-Doped Silica Nanoarchitecture Towards Electrochemical Sensing Ability

Olga Bochkova ^{1,*}, Mikhail Khrizanforov ¹, Aidar Gubaidullin ¹, Tatiana Gerasimova ¹, Irek Nizameev ¹, Kirill Kholin ¹, Artem Laskin ², Yulia Budnikova ¹, Oleg Sinyashin ¹ and Asiya Mustafina ¹

¹ Arbuzov Institute of Organic and Physical Chemistry, FRC Kazan Scientific Center, Russian Academy of Sciences, Arbuzov str., 8, 420088 Kazan, Russia; khrizanforov@gmail.com (M.K.); aidar@iopc.ru (A.G.); tatyana.gr@gmail.com (T.G.); irek.rash@gmail.com (I.N.); kholin06@mail.ru (K.K.); olefindirector@gmail.com (Y.B.); oleg@iopc.ru (O.S.); asiyamust@mail.ru (A.M.)

² Kazan Federal University, Kremlevskaya str. 29/1, 420008 Kazan, Russia; artemka166@mail.ru

* Correspondence: o.d.bochkova@mail.ru

Received: 17 June 2020; Accepted: 7 July 2020; Published: 9 July 2020



Abstract: The present work introduces both synthesis of silica nanoparticles doped with Co^{II} ions by means of differently modified microemulsion water-in-oil (w/o) and Stöber techniques and characterization of the hybrid nanoparticles (Co^{II}@SiO₂) by TEM, DLS, XRD, ICP-EOS, SAXS, UV-Vis, and UV-Vis/DR spectroscopy and electrochemical methods. The results reveal the lack of nanocrystalline dopants inside the hybrid nanoparticles, as well as no ligands, when Co^{II} ions are added to the synthetic mixtures as Co^{II}(bpy)₃ complexes, thus pointing to coordination of Co^{II} ions with Si-O groups as main driving force of the doping. The UV-Vis/DR spectra of Co^{II}@SiO₂ in the range of d-d transitions indicate that Stöber synthesis in greater extent than the w/o one stabilizes tetrahedral Co^{II} ions versus the octahedral ions. Both cobalt content and homogeneity of the Co^{II} distribution within Co^{II}@SiO₂ are greatly influenced by the synthetic technique. The electrochemical behavior of Co^{II}@SiO₂ is manifested by one oxidation and two reduction steps, which provide the basis for electrochemical response on glyphosate and HP(O)(OEt)₂ with the LOD = 0.1 μM and the linearity within 0.1–80 μM. The Stöber Co^{II}@SiO₂ are able to discriminate glyphosate from HP(O)(OEt)₂, while the w/o nanoparticles are more efficient but nonselective sensors on the toxicants.

Keywords: silica nanoparticles; cobalt (II) dopant; spectral properties; nanoarchitecture; organophosphorous compounds; electrochemical sensing

1. Introduction

Silica nanoparticles provide a good platform for uploading of metal ions and complexes through different synthetic approaches, including doping into silica matrix or deposition at a surface of nanoparticles [1–16]. Such hybrid silica nanoparticles uploaded by transition d-metal ions exhibit electrochemical behavior controlled by both inner-sphere environments of the metal ions and nano-architecture of the nanoparticles [14,15,17,18]. Controllable electrochemical behavior is a prerequisite for an application of the hybrid nanoparticles in electrochemical catalysis or sensing. In turn, nanoheterogeneous catalysts and sensors are of particular importance due to their greater stability and reusability versus the molecular complexes [14,15,17,18]. The substrate dependent electrochemical behavior of transition metal ions and complexes is the basis for electrochemical detection of many pollutants, including organophosphorous ones [19–29]. Electrochemical methods have many advantages over other sensing techniques such as reproducibility, good stability, high sensitivity,

measuring trace level of samples and cost-effectiveness [19,30,31]. This requires an engineering of new materials as components of electrodes with advanced electrochemical functions [32–34]. Both unique redox activity and easy encapsulation into polymeric materials make hybrid silica nanoparticles rather promising components of the electrodes for electrochemical sensing [35], although metal oxide or metal-based nanomaterials have got wider application in the engineering of the devices for electrochemical sensing [36,37]. Thus, design and synthesis of the hybrid nanoparticles with controllable inner-sphere environment of d-metal ions and their distribution within the nanoparticles is a rather challenging task from both fundamental and practical points of view.

However, successful doping or deposition of d-metal complexes without significant changes in the ligand environment can be performed only for kinetically inert complexes, which are exemplified in literature by tris-dipyridyles of Co^{III} and Ru^{II} [16,38–40]. The labile d-metal complexes, including those of Ni^{II} and Co^{II} , can also be doped into silica nanoparticles, although their ligand environment scarcely remains unchanged after the doping [14,15]. Moreover, literature data introduce both works reporting on safe doping of the Co^{II} complexes [2,9] and those revealing complex formation of Co^{II} ions with Si-O^- -groups as the reason for the ligand substitution [41]. The mutual impacts of electrostatic attraction of the complexes or coordinative bonding of Co^{II} ions with Si-O^- -groups to the doping procedure can be recognized by comparative structural analysis of the Co^{II} -dopants inside silica spheres. Thus, both $\text{Co}^{\text{II}}(\text{bpy})_3$ (bpy is 2,2'-bipyridine) and CoCl_2 will be used as the precursors for the synthesis of Co^{II} -doped silica nanoparticles.

The water-in-oil microemulsion (w/o) and Stöber procedures are most widely applied for doping of hydrophilic dopants such as d-metal salts or complexes into silica spheres [14–16,38–40]. As it was previously reported, the choice of w/o or Stöber procedure for doping of metal ions into silica nanoparticles has a great impact on both content of the dopants and their electrochemical and catalytic activity [14–16]. Thus, the present work is aimed at highlighting a role of the synthetic procedure and nature of the precursor on the structure of the Co^{II} -dopants and nanoarchitecture of Co^{II} -doped silica nanoparticles. In turn, the structural features of Co^{II} -dopants and Co^{II} -doped silica nanoparticles are correlated with their electrochemical behavior and sensing ability in order to reveal an applicability of the differently synthesized Co^{II} -doped silica nanoparticles for the sensing purposes. The water-in-oil microemulsion and Stöber procedures were chosen as the synthetic methods with the use of both $\text{Co}^{\text{II}}(\text{bpy})_3$ (bpy is 2,2'-bipyridine) and CoCl_2 as the precursors. The structural features of the hybrid silica nanoparticles were analyzed on both molecular and nano-levels by dynamic light and small angle X-ray scattering, electronic microscopy, elemental analysis and UV-Vis, UV-Vis DR, and IR spectroscopy methods. Electrochemical behavior of the hybrid nanoparticles was revealed in order to evaluate their applicability for the sensing. The sensing ability of the hybrid nanoparticles was exemplified by two organophosphorous compounds (OPC), which are the well-known pollutant glyphosate [42] and diethyl phosphite. The latter was chosen as a model of decomposition products of OPC, which are often no less toxic than the precursors.

2. Materials and Methods

2.1. Materials

Tetraethyl orthosilicate (TEOS, 98%), ammonium hydroxide (28–30%), n-heptanol (98%), cyclohexane (99%), 2,2'-bipyridine (bpy, 99%), diethyl phosphite (98%) were obtained from Acros Organics (Geel, Belgium); Triton X-100, cobalt(II) chloride (97%), cobalt(II) tetrafluoroborate hexahydrate (99%), N-(Phosphonomethyl)glycine (Glyphosate) were purchased from Sigma-Aldrich (St. Louis, Missouri, USA). CH_3CN (CHROMASOLV[®] Plus, $\geq 99.9\%$, by Acros Organics, Geel, Belgium) was used without any preliminary purification. The Ethanol, Acetone, and TEOS were purified by distillation.

$[\text{Co}(\text{bpy})_3](\text{BF}_4)_2$ was synthesized according to the known procedure [43]. To an ethanol solution of $\text{Co}(\text{BF}_4)_2 \cdot 6\text{H}_2\text{O}$ ($2 \times 10^{-2} \text{ mol} \cdot \text{L}^{-1}$) (100 mL), an ethanol solution (50 mL) of bpy ligand ($6 \times 10^{-2} \text{ mol} \cdot \text{L}^{-1}$)

was added under stirring. The resulting solution was stirred for 1 h, then filtered and left to evaporate at room temperature. After several days, air-stable, brown crystals of this complex were obtained. Yield: 83%. The elemental analysis data for $C_{30}H_{24}B_2CoF_8N_6$ are presented in Table 1. The spectroscopic data for $[Co(BF_4)_2(bpy)_3]$ matched that reported in the literature [43].

Table 1. The elemental analysis data for $C_{30}H_{24}B_2CoF_8N_6$.

Elements	C	H	B	Co	F	N
Anal. Calc., %	51.39	3.45	3.08	8.41	21.68	11.99
Found, %	51.41	3.41				

Et_4NBF_4 was obtained by mixing an aqueous solution of Et_4NOH (30–35%) with HBF_4 to a neutral indicator reaction. Et_4NBF_4 precipitated from the reaction mixture as white crystals, which were separated by filtering. The powder salt was further recrystallized from diethyl ether and dried for 2 to 3 days in a vacuum at 55 °C for dehydration.

Silica Nanoparticles Preparation

Water-in-oil (w/o) microemulsion procedure [44] was the following. A mixture of Triton X-100 (2.38 g), n-heptanol (2.29 mL), cyclohexane (9.32 mL), TEOS (0.2 mL), and 1.1 mL of bidistilled water (for “empty” silica nanoparticles) or aqueous solution (1.1 mL) of the Co^{II} -precursor ($Co(bpy)_3(BF_4)_2$ or $CoCl_2$, $C = 4.5 \times 10^{-3} \text{ mol} \cdot L^{-1}$) was prepared and stirred for 30 min. The obtained w/o microemulsion was mixed with a microemulsion containing Triton X-100 (2.38 g), n-heptanol (2.29 mL), cyclohexane (9.32 mL) and aqueous solutions of NH_3 (28–30%) with stirring. After 24 h of stirring, both Co^{II} -doped and empty silica nanoparticles were precipitated from the microemulsion by adding acetone with further centrifugation. The nanoparticle precipitate was washed by solutions of ethanol-acetone (1:1), ethanol (two times), and water (several times) to remove any residual surfactant molecules and organic solvents. Physically adsorbed Co^{II} ions or complexes and Triton X-100 molecules at nanoparticles surface were removed by ultrasonication during the washing procedure. Pink-colored Co^{II} -doped and white “empty” silica nanoparticles were obtained.

Stöber synthesis [14] was done through the following steps. A solution of TEOS (1.14 mL) in EtOH (11.36 mL) was added to NH_4OH (28–30%) (0.38 mL) in EtOH (8.05 mL)- H_2O (4.05 mL) at the speed 2 mL per min (thought syringe pump) under continuous stirring (750 rpm). After 6 min, the solution of $[Co(bpy)_3](BF_4)_2$ or $CoCl_2$ in EtOH (2.5 mL, $C = 4.5 \times 10^{-3} \text{ mol} \cdot L^{-1}$) was injected into this mixture. In the case of the “empty” silica nanoparticles, the solution of TEOS (1.14 mL) in EtOH (11.36 mL) was added to NH_4OH (28–30%) (0.38 mL) in EtOH (10.55 mL)- H_2O (4.05 mL) at the speed 2 mL per min (thought syringe pump) under continuous stirring (750 rpm). After 6 h of stirring, silica nanoparticles were precipitated by centrifuging and washing several times by ethanol and water. To remove physically absorbed Co^{II} complexes or ions from the particles surfaces, an ultrasonication was used during the washing procedure. Blue-colored Co^{II} -doped and white “empty” silica nanoparticles were obtained.

The electrochemical, PXRD, SAXS, IR, and Raman experiments were performed with dried samples of the silica nanoparticles.

2.2. Samples Characterization

Transmission electron microscopy (TEM) measurements were carried out on Hitachi HT7700 transmission electron microscope (Chiyoda-ku, Japan) with energy-dispersive X-ray detector from Thermo Scientific. The accelerating voltage was equal to 80 kV. The accumulation time of one spectrum was 300 s.

Co and Si were identified in the silica nanoparticles colloids using a simultaneous inductively coupled plasma atomic emission spectrometry (ICP-AES) model iCAP 6300 DUO by Varian Thermo Scientific Company equipped with a CID detector. This spectrometer enables the simultaneous

measurement of peak heights within the 166 to 867 nm range. The optical resolution is less than 0.007 nm to 200 nm. As for the working frequency, it is 27.12 MHz. Together, the radial and axial view configurations enable optimal peak height measurements with suppressed spectral noises.

UV-Vis spectra of solutions and silica nanoparticles dispersions were recorded on Specord^R50 Plus (Analytikjena, Germany). SNs dispersions were ultrasonicated within 10 min before using.

Powdered samples were characterized by UV-Vis/DR technique using a Jasco V-650 spectrophotometer (Jasco International Co. Ltd., Hachioji, Tokyo, Japan) equipped with an integrating sphere accessory for diffuse reflectance spectra acquisition. BaSO₄ powder was used as the reference for baseline correction.

The dynamic light scattering (DLS) measurements were performed by means of the Malvern Mastersize 2000 particle analyzer (Malvern, UK). A He-Ne laser operating at 633 nm wavelength and emitting vertically polarized light was used as a light source. The measured autocorrelation functions were analyzed by Malvern DTS software and the second-order cumulant expansion methods. The effective hydrodynamic radius (RH) was calculated by the Einstein–Stokes relation from the first cumulant: $D = kBT/6\eta RH$, where D is the diffusion coefficient, kB is the Boltzmann constant, T is the absolute temperature, and η is the viscosity. The diffusion coefficient was measured at least three times for each sample. The average error in these experiments was approximately 4%. All samples were prepared from the bidistilled water with prior filtering through the PVDF membrane using the Syringe Filter (0.45 μm). Zeta potential “Nano-ZS” (MALVERN) using laser Doppler velocimetry and phase analysis light scattering was used for zeta potential measurements. Silica nanoparticles dispersions were ultrasonicated within 10 min before using.

IR spectra of solid samples have been registered using a Bruker Vector-27 FTIR spectrometer in the 400–4000 cm^{-1} range (optical resolution 4 cm^{-1}). The samples were prepared as KBr pellets.

Raman spectra were registered at room temperature using a BRUKER RAM II module attached to a BRUKER VERTEX 70 FTIR spectrometer (excitation 1064 nm, Ge detector at liquid nitrogen temperature, back-scattering configuration; range 10–4000 cm^{-1} , optical resolution 4 cm^{-1} , scan number 1024).

Electrochemical measurements were taken on a BASiEpsilonE2P electrochemical analyzer (West Lafayette, IN, USA). The program concerned Epsilon-ECUSB-V200 waves. A conventional three-electrode system was used with glassy carbon for carbon paste electrode (CPE) solutions for powder samples as the working electrode, the An Fc/Fc system serving as reference electrode, and a Pt wire as the counter electrode. In addition, 0.1 M [Et₄N][BF₄] was used as the supporting electrolyte to determine the current voltage characteristics. The solvent for all measurements was water. To study the powder samples, a modified CPE working electrode was used, which was prepared as follows: the carbon particles/phosphonium salt (dodecyl(tri-tert-butyl)phosphonium tetrafluoroborate) composite electrode was prepared using a grinding a mixture of graphite powder and phosphonium salt with a 90/10 (w/w) ratio in mortar giving it a homogeneous mass [45]. A modified electrode was also devised in a similar manner except that a portion (ca. 5%) of the graphite powder was replaced by the CPs under study. As a result, a portion of the resulting paste was packed firmly into the (3 mm in diameter) Teflon holder cavity.

Powder X-ray diffraction (PXRD) measurements were performed on a Bruker D8 Advance diffractometer equipped with Vario attachment and Vantec linear PSD, using Cu radiation (40 kV, 40 mA) monochromated by the curved Johansson monochromator (λ Cu K $_{\alpha 1}$ 1.5406 Å). Room-temperature data were collected in the reflection mode with a flat-plate sample. The samples were loaded on a standard zero diffraction silicon plate, which was kept spinning (15 rpm) throughout the data collection. Patterns were recorded in the 2Θ range between 3° and 93°, in 0.008° steps, with a step time of 0.1–4.0 s. Several diffraction patterns in various experimental modes were collected and summed for the sample. Processing of the obtained data performed using EVA software packages [46].

Small angle X-Ray scattering (SAXS) data for samples were collected with the Bruker AXS Nanostar system using CuK α (λ 1.5418 Å) radiation from a 2.2 kW X-ray tube (40 kV, 35 mA) coupled with Gobbel mirrors optics and a HiStar 2D area detector. The beam was collimated using three pinholes

with apertures of 800, 450, and 700 μm . The instrument was operated with a sample-to-detector distance of 63.5 cm to provide data at angles $0.1^\circ < 2\theta < 4.8^\circ$, which correspond to $0.007 \text{ \AA}^{-1} < s < 0.34 \text{ \AA}^{-1}$. The value of s is proportional to the inverse of the length scale ($s = (4\pi/\lambda)\sin(\theta)$ in units of \AA^{-1}). Scattering patterns were obtained for the samples at 23 $^\circ\text{C}$ in an evacuated chamber. The measurements were performed in transmission mode with the use of glass capillaries filled by powder samples. The capillaries (2 mm diameter) were sealed and put into evacuated chamber by means of the holders. For each sample, several experiments were performed, allowing for controlling the quality of the experiments. The results of the experiments are summarized, so that the total time of each experiment was equal to 30,000 s. The 2D scattering patterns were integrated using the SAXS program package [47]. Calculation of structural parameters, simulation, and graphical representation of the results were performed using a PRIMUS [48] program package.

3. Results and Discussion

3.1. Size, Cobalt Content, and Spectral Properties of the Hybrid Nanoparticles (CoII@SiO_2) in Correlation with the Synthetic Conditions

Stöber and water-in-oil microemulsion (w/o) techniques provide a facile approach for encapsulation of charged metal complexes into silica nanoparticles [2,9,14–16,38–40]. The use of the both techniques results in the synthesis of the hybrid silica nanoparticles. Figure 1 illustrates the TEM images of the hybrid nanoparticles, while their diameters evaluated from the images and the Si:Co ratios calculated from the ICP-EOS data are collected in Table 2. The data in Table 1 indicate that the size and the content of Co^{II} evaluated by the Si:Co ratios are to a major extent dependent on the synthetic technique, while smaller differences derive from the doping of $\text{Co}^{\text{II}}(\text{bpy})_3$ or CoCl_2 . The difference in the synthetic methods is illustrated by Scheme 1. The size of the nanoparticles synthesized by the w/o technique is controlled by the TX-100-based reverse micelles (Scheme 1). Thus, water:oil volume ratios along with surfactant and co-surfactant concentrations have a great impact on the size control in the framework of the w/o technique. The sizes of silica nanoparticles grown by the Stöber method are mainly affected by concentrations of TEOS and ammonia, while the ethanol:water volume ratio plays a smaller role in controlling the size (Scheme 1). Moreover, the water soluble Co^{II} -dopants are concentrated within nano-droplets of the reverse micelles, which explains the greater uploading by Co^{II} ions for the nanoparticles synthesized by the w/o procedure in comparison with those obtained by the Stöber method (Table 2, Scheme 1). It is also worth noting that the color of both aqueous colloids and dried samples of the hybrid nanoparticles are pink when they are synthesized by the w/o, while the Stöber procedure results in the blue nanoparticles. Similar to the above-mentioned factors the color of the hybrid nanoparticles seems to be independent from their doping with $\text{Co}^{\text{II}}(\text{bpy})_3$ or CoCl_2 .

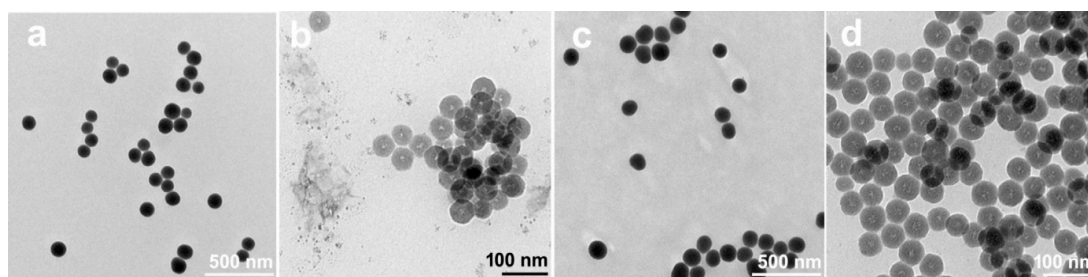
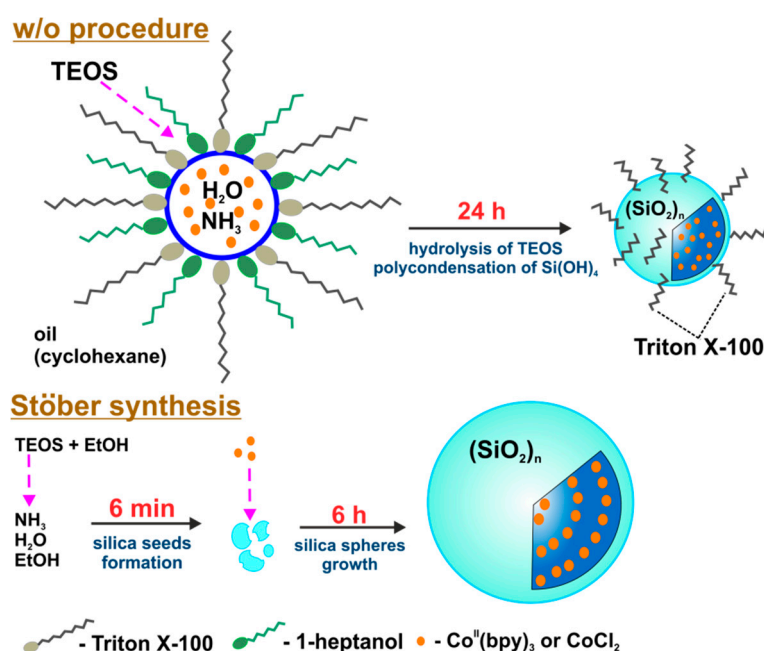


Figure 1. TEM-images of $\text{Co}^{\text{II}}\text{@SiO}_2$ nanoparticles obtained by: Stober procedure (a,c) and water-in-oil microemulsion technique (b,d) on the basis of $\text{Co}^{\text{II}}(\text{bpy})_3$ (a,b) and CoCl_2 (c,d) as dopants.

Table 2. Average diameters (d) in dried samples (TEM), Si:Co molar ratio (ICP-OES), average hydrodynamic diameters (D), polydispersity index (PDI) and zeta potential values (ζ) (DLS) in aqueous colloids of the differently synthesized $\text{Co}^{\text{II}}@ \text{SiO}_2$ ($C = 0.2 \times \text{g} \cdot \text{L}^{-1}$).

Synthetic Method, Precursor	d, nm	Si:Co Molar Ratio, %	D, nm	PDI	ζ , mV
Stöber, $\text{Co}^{\text{II}}(\text{bpy})_3$	109 ± 20	100:0.243	225 ± 2	0.139	-51 ± 1
w/o, $\text{Co}^{\text{II}}(\text{bpy})_3$	50 ± 5 ¹	100:0.680	144 ± 1	0.114	-29 ± 1
Stöber, CoCl_2	118 ± 10	100:0.130	154 ± 1	0.144	-51 ± 1
w/o, CoCl_2	43 ± 3	100:0.578	118 ± 2	0.117	-38 ± 1

¹ TEM image (Figure 1b) reveals an admixture of the small (2–5 nm) nanoparticles.



Scheme 1. Schematic representation of different techniques for synthesis of $\text{Co}^{\text{II}}@ \text{SiO}_2$.

The presence of bpy ligands both coordinated with $\text{Co}(\text{II})$ and as “free” molecules inside silica nanoparticles can be revealed by UV-Vis spectroscopy measurements in both supernatants (Figure 2b) and aqueous dispersions of the synthesized silica nanoparticles (Figure 2a). The analysis of the UV-Vis spectral data reveals the lack of the bands peculiar for $\text{Co}^{\text{II}}(\text{bpy})_3$ in the aqueous colloids for both types of $\text{Co}^{\text{II}}@ \text{SiO}_2$ (curves 2 and 3 in Figure 2a). The supernatant after the synthesis by the Stöber procedure reveals the release of bpy from the complex (Figure 2b), while the electronic absorption bands of Triton X-100 mask the presence of bpy in the supernatant after the synthesis by the w/o method (Figure S1). Moreover, its concentration in the supernatant indicates the degradation of about 57% of $\text{Co}^{\text{II}}(\text{bpy})_3$ added to the synthetic mixture.

Thus, the color changes during the synthesis of the nanoparticles by the w/o and Stöber procedures derive from the transformation of the spectral pattern from $\text{Co}^{\text{II}}(\text{bpy})_3$ to that of bpy (Figure 3). In particular, the yellow color seems to remain unchanged in aqueous or alcohol solution of $\text{Co}(\text{bpy})_3(\text{BF}_4)_2$ exactly after addition of tetraethoxysilane and ammonia (4–8 in Figure 3), which is confirmed by the small changes in the spectral pattern of $\text{Co}^{\text{II}}(\text{bpy})_3$. The color changes followed by the spectral transformations from that of $\text{Co}^{\text{II}}(\text{bpy})_3$ to that of bpy (3 and 1 in Figure 3) is observed within 6 or 30 min after beginning of the Stöber (9 in Figure 3) or w/o synthesis. The time durations for 6 and 30 min correlate with the appearance of silica seeds in the framework of Stöber [14,39] and w/o [49] procedures. It is worth assuming that the growth of silica seeds with Si-O^- groups exposed at their surface provides a reason for the transformations of $\text{Co}^{\text{II}}(\text{bpy})_3$ to bpy and Co^{II} ions due to a

complex formation of the latter with Si-O⁻ groups of the silica seeds. The assumption can be confirmed by comparison of the UV-Vis diffuse reflectance spectra in the long-wave spectral range derived from the d-d transitions of the hybrid nanoparticles doped with Co(dipy)₃(BF₄)₂ or CoCl₂ (Figure 4). For these purposes, the UV-Vis/DR spectra of Co^{II}@SiO₂ were recorded for their dried samples along with the powder of Co(dipy)₃(BF₄)₂ (Figure 4) and “empty” silica spheres (SiO₂) (Figure S2) for the comparison. The latter were synthesized by the same w/o and Stöber procedures without the addition of the Co^{II}-dopants. The characterization of SiO₂ synthesized in the same synthetic conditions as the Co^{II}@SiO₂ by TEM indicate that their sizes are greatly affected by the synthetic method (48 ± 5 and 97 ± 5 nm for SiO₂ synthesized by w/o and Stöber methods correspondingly), while the effect of the dopants is rather small (compare with the sizes in Table 2).

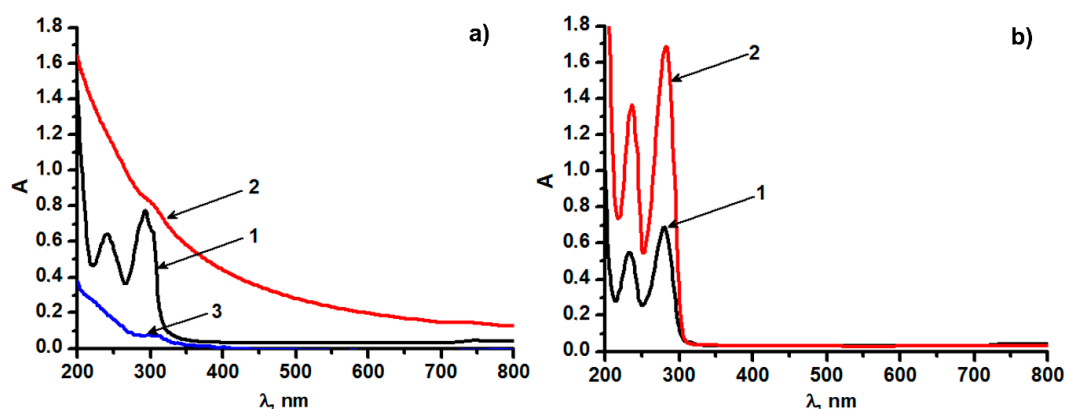


Figure 2. UV-Vis absorbance spectra in ethanol of: (a) 1—Co(bpy)₃(BF₄)₂ ($C = 1.67 \times 10^{-5} \text{ mol}\cdot\text{L}^{-1}$), Co^{II}@SiO₂ ($C = 0.2 \text{ g}\cdot\text{L}^{-1}$) on the basis of Co^{II}(bpy)₃ obtained by different techniques: 2—Stöber, 3—w/o; (b) 1—bpy ($C = 5 \times 10^{-5} \text{ mol}\cdot\text{L}^{-1}$), 2—supernatant after Stöber synthesis diluted 10 times.

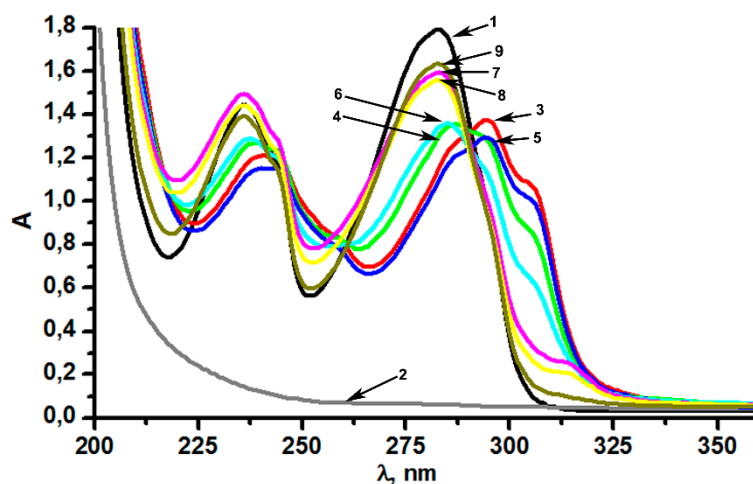


Figure 3. UV-Vis absorbance spectra in ethanol of: 1—bpy ($C = 5 \times 10^{-5} \text{ mol}\cdot\text{L}^{-1}$); 2—TEOS; 3—Co(bpy)₃(BF₄)₂ ($C = 4 \times 10^{-5} \text{ mol}\cdot\text{L}^{-1}$); Co^{II}(bpy)₃ ($C = 4 \times 10^{-5} \text{ mol}\cdot\text{L}^{-1}$) in the presence of: 4—ammonia hydroxide, 5—TEOS, 6—NH₄OH and TEOS, 7—NH₄OH after 40 min of stirring, 8—NH₄OH and TEOS after 40 min of stirring (Co:TEOS:NH₃ ratio was the same as in the Stöber synthetic conditions); 9—Co^{II}(bpy)₃ after addition in the synthetic mixture according to synthesis condition (Stöber synthesis in Materials and Methods section) and this mixture was diluted 10 times.

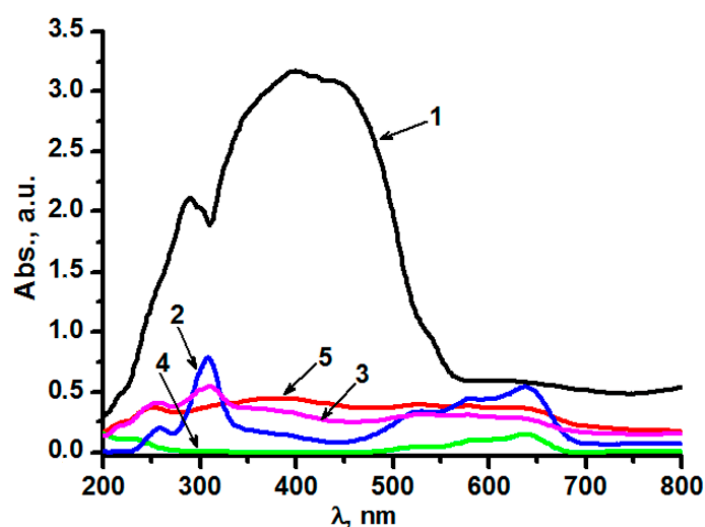


Figure 4. UV-Vis diffuse reflectance spectra of: $\text{Co}^{\text{II}}(\text{bpy})_3$ (1); and $\text{Co}^{\text{II}}@ \text{SiO}_2$ synthesized by different techniques: Stöber with $\text{Co}^{\text{II}}(\text{bpy})_3$ (2) and CoCl_2 (4); w/o with $\text{Co}^{\text{II}}(\text{bpy})_3$ (3) and CoCl_2 (5).

The spectra in Figure 4 indicate the difference in the spectral pattern within 500–700 nm for the $\text{Co}^{\text{II}}@ \text{SiO}_2$ synthesized by the w/o and Stöber procedures, while the nature of the Co^{II} -precursor ($\text{Co}(\text{bpy})_3(\text{BF}_4)_2$ or CoCl_2) insignificantly affects the d-d transitions of the $\text{Co}^{\text{II}}@ \text{SiO}_2$. The spectra of $\text{Co}^{\text{II}}@ \text{SiO}_2$ synthesized with the use of $\text{Co}^{\text{II}}(\text{bpy})_3$ as precursor (2 and 3 in Figure 4) differ from the one of $\text{Co}^{\text{II}}(\text{bpy})_3$ complex in the range associated with d-d transitions, but demonstrate the band at ~300 nm, absent in the spectra of $\text{Co}^{\text{II}}@ \text{SiO}_2$ with CoCl_2 (curve 4 and 5 in Figure 4), associated most probably with “free” bpy. The spectra of the Stöber $\text{Co}^{\text{II}}@ \text{SiO}_2$ (curve 2 and 4 in Figure 4) demonstrate three strong bands at 528, 580, and 638 nm, which are characteristic for ${}^4\text{A}_2(\text{F}) \rightarrow {}^4\text{T}_1(\text{P})$ transitions in tetrahedral Co^{II} chromophores [50–53]. It should be mentioned that the same spectral pattern (bands at 547, 585, 633 nm) has been observed for tetrahedral Co^{II} ion coordinated to four oxygen atoms in 1D coordination polymer of $\text{Co}(\text{fcdHp})$, based on 1,1'-ferrocenylenbis(H-phosphinic) acid (H_2fcdHp) [54]. The similar bands in this region (curve 3 and 5 in Figure 4) are not so pronounced in the spectra of the w/o $\text{Co}^{\text{II}}@ \text{SiO}_2$. They also demonstrate another rearrangement of intensities. Most probably, the spectral pattern of the w/o $\text{Co}^{\text{II}}@ \text{SiO}_2$ samples derives from Co^{II} ions in octahedral environment, for which weak bands at ca. 500–580 nm assigned to ${}^4\text{T}_{1g} \rightarrow {}^4\text{A}_{2g}(\text{F})$ transitions are characteristic [50,53,55]. The absorbance intensity of tetrahedral Co^{II} is more intense (~100 times) than that of octahedral Co^{II} due to the lack of an inversion center in the former symmetry [56]. Therefore, the contribution from the octahedral Co^{II} to the spectral pattern could be masked by the bands arisen from the tetrahedral Co^{II} chromophores. Nevertheless, both rearrangement of bands intensities at 500–700 nm and their lowering in spectra 3 and 5 compared to 2 and 4 (Figure 4) allows one to suggest the greater contribution of the octahedral Co^{II} chromophores in the w/o $\text{Co}^{\text{II}}@ \text{SiO}_2$ versus the Stöber $\text{Co}^{\text{II}}@ \text{SiO}_2$. It is noteworthy that the coordinative bonds between the Co^{II} ions and Si-O^- groups at the silica surface are the key reason for the formation of the $\text{Co}^{\text{II}}@ \text{SiO}_2$ by the w/o and the Stöber procedures. However, it is worth assuming that the extents of tetrahedral and octahedral Co^{2+} chromophores are greatly affected by the aqueous or alcohol environment of Co^{II} ions in the frameworks of the w/o or Stöber techniques (Scheme 1).

The infrared and Raman spectra of $\text{Co}^{\text{II}}@ \text{SiO}_2$ nanoparticles (Figure 5) synthesized by both methods are very similar and demonstrate characteristic for silica nanoparticles bands: 475 cm^{-1} , attributed to bending modes between the Si-O-Si bonds, 800 cm^{-1} , assigned to the symmetric stretching vibration between Si-O-Si bonds, $\sim 960 \text{ cm}^{-1}$ that is often linked with the stretching vibration of Si-OH bond and $\sim 1100 \text{ cm}^{-1}$, which corresponds to the asymmetric stretching vibration of Si-O-Si bond in the SiO_4 tetrahedron as reported in literature [41,57–60]. The IR spectra of NPs obtained by the

w/o technique (cyan and red in Figure 5a) contain additional bands at ~ 1370 , 1701 , and 2930 cm^{-1} most probably associated with CH bending and C=O and alkyl CH stretching vibrations of acetone and TX-100 molecules (cyan and red in Figure 5a). The presence of TX-100 molecules derives from their efficient adsorption at the surface of silica nanoparticles (Scheme 1) leading to the so-called surfactant-based corona similar with the previously reported F-127-based corona [61] of the silica nanoparticles synthesized by the w/o procedure with F-127 as the surfactant. Raman spectra of Stöber $\text{Co}^{\text{II}}@\text{SiO}_2$ based on $\text{Co}^{\text{II}}(\text{bpy})_3$ contain very weak bands of bpy at ~ 1600 and 1570 cm^{-1} (magenta in Figure 5b), which are absent in the spectrum of “empty” SiO_2 (black in Figure 5b), and are not visible in their IR spectra (magenta in Figure 5a).

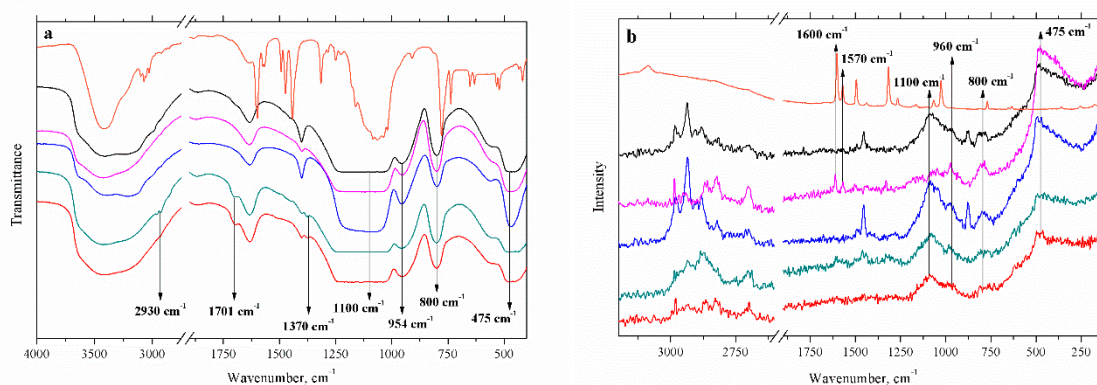


Figure 5. IR (a) and Raman (b) spectra of $\text{Co}^{\text{II}}(\text{bpy})_3$ (orange), SiO_2 (black) and $\text{Co}^{\text{II}}@\text{SiO}_2$ synthesized by the w/o on the basis of $\text{Co}^{\text{II}}(\text{bpy})_3$ (cyan) and CoCl_2 (red) and by Stöber on the basis of $\text{Co}^{\text{II}}(\text{bpy})_3$ (magenta) and CoCl_2 (blue).

3.2. Nanoarchitecture of $\text{Co}^{\text{II}}@\text{SiO}_2$ and SiO_2 in Correlation with the Synthetic Procedure

Electrochemical behavior of metal ions encapsulated into silica nanoparticles is affected by the inner-sphere environment of metal ions and their preferable localization within interior (core) or exterior (shell) zones of the hybrid nanoparticles [15,62]. Thus, nanoarchitecture of the hybrid nanoparticles manifested by different distribution of the dopant within their core and shell zones was studied by powder X-ray diffraction (PXRD) and small angle X-ray scattering (SAXS) techniques. Combination of the techniques was used to reveal both supramolecular and nano-structuring in the dried samples of $\text{Co}^{\text{II}}@\text{SiO}_2$ and SiO_2 synthesized by the both methods. It is well-known that silica spheres synthesized by w/o or Stöber techniques are manifested by widened peaks in PXRD spectra, while the presence of nano-crystallites derived from the cobalt salts or oxides can be revealed by the appearance of the specific peaks [41,62,63]. Literature data indicate that the amorphous nature of silica remains practically unchanged under coordination of Co(II) ions with Si-O⁻ groups, while the narrow peaks revealing the nanocrystallites of cobalt oxide derive from the extra-amounts of the doped cobalt salt [41,62]. Such nanocrystallites can be revealed by comparative analysis of PXRD data of $\text{Co}^{\text{II}}@\text{SiO}_2$ nanoparticles synthesized by both methods and their empty analogous (SiO_2). The PXRD spectra recorded for the dried samples of $\text{Co}^{\text{II}}@\text{SiO}_2$ and SiO_2 nanoparticles synthesized by the both methods (Figure 6) demonstrate the PXRD patterns peculiar for amorphous silica nanoparticles, which agrees well with the concentration conditions in the synthesis of the $\text{Co}^{\text{II}}@\text{SiO}_2$ (see the Exp. Section for more details). However, the weak widened peaks in the range of small angles revealed in the PXRD curves of Stöber $\text{Co}^{\text{II}}@\text{SiO}_2$ and SiO_2 derive from the inclusions of paracrystalline phase with short- and medium-range ordering into the amorphous nanoparticles.

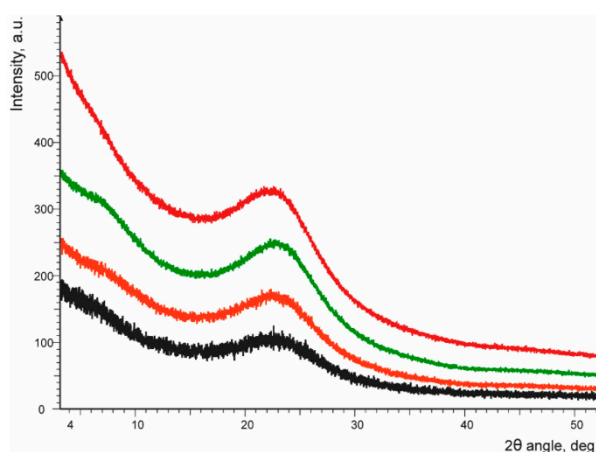


Figure 6. PXRD patterns: black—w/o SiO₂, orange—Stöber SiO₂, red—w/o Co^{II}@SiO₂, green—Stöber Co^{II}@SiO₂. The curves are shifted relative to each other along the intensity axis for clarity.

SAXS has been previously documented as successful technique to reveal nano-structuring deriving from silica nanoparticles, as well as inhomogeneity in electron density distribution within nanoparticles [41,64–66]. It is worth noting in this connection that the sizes of Co^{II}@SiO₂ and SiO₂ nanoparticles synthesized by Stöber method (Tables 2 and 3) lie above the values available for correct evaluation by the method (1–60 nm), while the sizes of smaller Co^{II}@SiO₂ and SiO₂ nanoparticles synthesized by the w/o procedure can be evaluated from the SAXS measurements. However, the X-ray scattering profiles of the Co^{II}@SiO₂ and SiO₂ (Figure S3) reveal their nanostructuring manifested by the presence of nano-aggregates with the sizes below 60 nm even for the Stöber Co^{II}@SiO₂ and SiO₂. The nanostructuring arisen from inhomogeneity of electron density distribution within the silica nanoparticles may be quantitatively described in a “core-shell” framework. However, the shell zones of such “core-shell” nanoparticles along with the interparticle space can be considered as isotropic homogeneous medium with the electron density lower than that of the core zone. It is worth assuming that the core zones of the Co^{II}@SiO₂ and SiO₂ as nanoparticles encapsulated into an isotropic medium with distances between their centers above the sizes of the core zones. Thus, the quantitative analysis of the SAXS data was performed in the assumption that the scattering results from noninteracting spherical nanoparticles uniformly enclosed in a homogeneous medium which provides their local monodisperse environment. Two-dimensional scattering curves were obtained by averaging of the eight X-ray scattering measurements for both hybrid and empty silica nanoparticles, while no effect of the prolonged X-ray irradiation on the scattering data was revealed (Figure S4).

Table 3 collects the calculated from the SAXS data parameters characterizing nanoparticles, such as radius of gyration (R_g and R_g^*) evaluated by the Guinier method and from analysis of distance distribution function respectively, biggest distances in the particles (D_{max}), and average diameter of the particles in a sphere-shaped model framework (d_s , $d_s = \sqrt{5/3} \times R_g \times 2$). The latter can be compared with the d -values evaluated by TEM, which are also collected in Table 2 to facilitate the comparison. This difference is too great to be explained by the difference in the techniques. The d_s values calculated from SAXS are at the level of 33–38 nm for Co^{II}@SiO₂ and SiO₂ nanoparticles synthesized by the w/o technique; these values are lower than the d values evaluated by TEM on about 10 nm (Table 3). In the framework of the aforesaid assumption, the sizes revealed by the SAXS measurements refer to the core zones of the w/o Co^{II}@SiO₂ and SiO₂. This doesn't exclude the presence of an exterior layer exhibiting smaller electronic density than the silica spheres. The above-mentioned TX-100-corona at the surface of w/o Co^{II}@SiO₂ and SiO₂ is one of the reasons for an exterior layer with the electron density smaller than that arisen from the silica matrix. Therefore, the deviation between the d_s and d values can be explained by the fact that the sizes revealed by the TEM images derive from both core and shell zones of the w/o Co^{II}@SiO₂ and SiO₂. It is also worth noting that the D_{max} values exceed the d_s ones on

no more than 5 nm (Table 3), which, in turn, indicates that the shape of the w/o Co^{II}@SiO₂ and SiO₂ revealed by SAXS deviates from an ideal spherical shape.

Table 3. The R_g , R_g^* , D_{max} , d_s , FD, and V_{part} (averaged particle volume) values, the scattering intensity at $q = 0$ (I_0 , in arbitrary units), and the diameters of Co^{II}@SiO₂ and SiO₂ nanoparticles synthesized by the both methods (d^{TEM} obtained by TEM method) are presented for the comparison.

Sample (Technique, Precursor)	R_g , Å	R_g^* , Å	D_{max} , nm	V_{part} , Å ³	I_0 , a.u.	d_s , nm	FD	d^{TEM} , nm
w/o, CoCl ₂	131.0 ± 6	130.9 ± 7	39.4 ± 0.6	122 × 10 ⁵	166000	33.8 ± 1.8	3.41	43 ± 3
w/o, Co ^{II} (bpy) ₃	145.5 ± 7	145.6 ± 5	43.4 ± 0.7	148 × 10 ⁵	229900	37.6 ± 1.3	3.29	50 ± 5
Stöber, CoCl ₂	164.6 ± 7	164.4 ± 8	50.1 ± 0.7	236 × 10 ⁵	84660	41.4 ± 2.1	2.61	118 ± 10
Stöber, Co ^{II} (bpy) ₃	139.4 ± 6	139.4 ± 7	43.7 ± 0.6	133 × 10 ⁵	60640	36.0 ± 1.8	2.69	109 ± 20
w/o, "empty"	128.0 ± 6	127.8 ± 7	36.4 ± 0.6	114 × 10 ⁵	183600	33.0 ± 1.8	3.53	48 ± 5
Stöber, "empty"	132.7 ± 8	132.6 ± 6	37.1 ± 0.6	101 × 10 ⁵	143200	34.0 ± 1.5	3.37	97 ± 5

The evaluated from the SAXS data fractal dimensions (FD) of w/o Co^{II}@SiO₂ and SiO₂ presented in Table 3 are above 3.0. Such FD values are peculiar for surficial fractality derived from the folded surface, whose density is lower than that of the silica matrix. This is in good agreement with the aforesaid assumption about the TX-100-based corona at the silica surface as schematically shown in Scheme 1. Comparative analysis of both FD and R_s values reveals the insignificant difference between "empty" SiO₂ and Co^{II}@SiO₂ w/o nanoparticles (Table 3). This similarity indicates that the distribution of the Co^{II} ions within Co^{II}@SiO₂ (w/o) is rather homogeneous without preferable localization within specific zones of the nanoparticles, while the lower electronic density of the exterior layer derives from the specificity of the w/o technique (Scheme 1).

The SAXS analysis of Stöber Co^{II}@SiO₂ and SiO₂ is the peculiar case, since the greatest R_g values refer to the d_s -values at the level of 34–41 nm which are far below the d -values evaluated from the TEM images (Table 3, Figure S5). Moreover, more smooth profiles of the scattering curves measured for Stöber Co^{II}@SiO₂ and SiO₂ in comparison with the w/o ones (Figure S3) indicate greater polydispersity of the Stöber versus the w/o nanoparticles. This deviation points to inhomogeneity in electron density distribution within Stöber Co^{II}@SiO₂ and SiO₂, which agrees well with the zones of short- and medium-range ordering revealed from the PXRD curves of the corresponding nanoparticles (Figure 6). The shapes of the revealed core zones also deviate from ideal spheres, which is evident from the deviation between D_{max} and d_s values (Table 3). Moreover, the FD value of the empty silica spheres made by Stöber procedure is on the level of surficial fractality (3.37), while the FD values of the Stöber Co^{II}@SiO₂ (2.6–2.7) refer to the so-called mass fractality which indicate the inhomogeneous distribution of Co^{II} ions within the Stöber Co^{II}@SiO₂. This is quite different from the homogeneous distribution within the w/o Co^{II}@SiO₂, where both FD and d_s values of the "empty" SiO₂ and Co^{II}@SiO₂ nanoparticles are at the same level.

In summary, the SAXS data revealed that the synthesis of Co^{II}@SiO₂ in the framework of Stöber method results in the localization of Co^{II}-dopant within specific zones of the silica spheres, while more homogeneous distribution of Co^{II}-dopant within Co^{II}@SiO₂ is obtained by the w/o technique. Moreover, the surface fractality of Co^{II}@SiO₂ (w/o) can be explained by the porous silica surface decorated by TX-100-based corona.

3.3. Electrochemical Behavior of Co^{II}@SiO₂

The electrochemical behavior of Co^{II}@SiO₂ was measured with the use of carbon-paste electrode (CPE) [45]. The CPE-based technique enables avoiding effects of different colloid stability, which makes it most convenient for comparative analysis of electrochemical behavior of Co^{II} encapsulated into Co^{II}@SiO₂ synthesized by the Stöber and w/o methods. Two types of Co^{II}@SiO₂, i.e., (Stöber) and (w/o) have identical first oxidation and reduction peaks. In particular, one-electron irreversible oxidation of Co^{II} to Co^{III} is observed at a potential of 0.65 V (Figure 7). At −1.12–1.15 V, a one-electron reversible reduction of Co^{II} to Co^I is observed for both types of nanoparticles, while a significant difference is

observed at the second reduction of Co^{I} to Co^0 peak. The irreversible reduction of Co^{I} to Co^0 recorded at -1.69 V is revealed for Stöber $\text{Co}^{\text{II}}@/\text{SiO}_2$, while, for w/o $\text{Co}^{\text{II}}@/\text{SiO}_2$, the reduction at -1.38 V is reversible (Figure 7, Table 4).

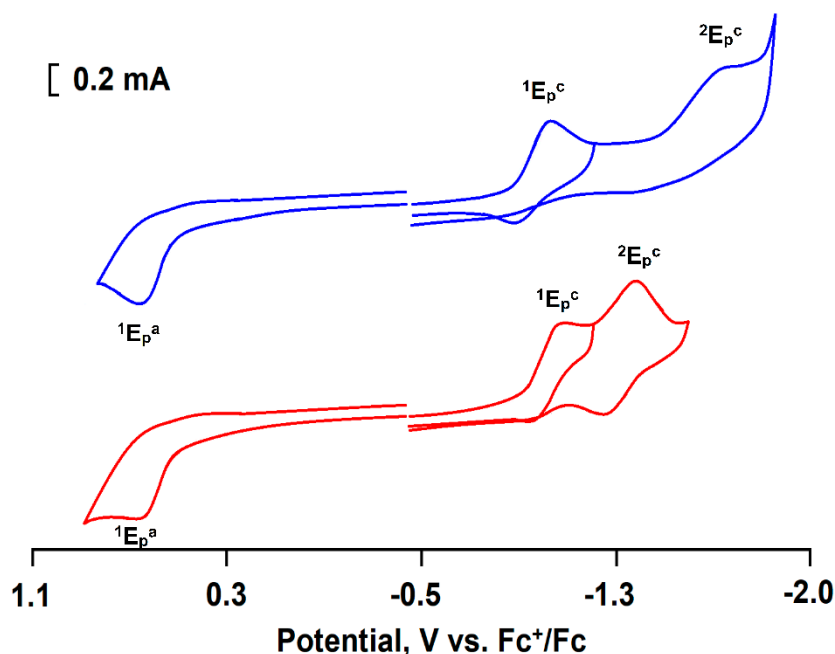


Figure 7. CVs for w/o $\text{Co}^{\text{II}}@/\text{SiO}_2$ (red) and Stöber $\text{Co}^{\text{II}}@/\text{SiO}_2$ (blue) WE: CPE, H_2O , 10^{-1} mol·L $^{-1}$ Et_4NBF_4 Potentials vs. Ag/AgCl recalculated to Fc^+/Fc .

Table 4. The potentials for Figure 7. Conditions: 25 °C, working electrode: CPE (graphite + ionic liquid + [Co particles]), Et_4NBF_4 background salt, H_2O , 100 mV/s. Potentials vs. Fc^+/Fc .

Sample	Reduction		Oxidation
	$^1\text{E}_p^c/\text{E}_p^a$, V	$^2\text{E}_p^c/\text{E}_p^a$, V	$^1\text{E}_p^a/\text{E}_p^c$, V
Stöber $\text{Co}^{\text{II}}@/\text{SiO}_2$	$-1.12/-0.90$	$-1.69/\text{irrev}$	$0.71/\text{irrev}$
w/o $\text{Co}^{\text{II}}@/\text{SiO}_2$	$-1.15/-0.99$	$-1.38/-1.26$	$0.72/\text{irrev}$

It is well-known that reduction or oxidation potentials are to a great extent dependent on the inner-sphere environment of Co^{II} . However, the previous report reveals that predominant localization of the Ni^{II} complexes within core zone of the Ni^{II} -doped silica nanoparticles shifts the electrochemical Ni^{II} to Ni^{I} reduction to more negative potentials [15]. Thus, the second Co^{I} to Co^0 reduction step is affected, while the Co^{II} to Co^{I} reduction and Co^{II} to Co^{III} oxidation potentials are not influenced by the synthetic method (Table 4). The results are not enough to recognize the exact reasons for the aforesaid similarities and differences in electrochemical behavior of Stöber $\text{Co}^{\text{II}}@/\text{SiO}_2$ and w/o $\text{Co}^{\text{II}}@/\text{SiO}_2$. Nevertheless, the electrochemical activity of the $\text{Co}^{\text{II}}@/\text{SiO}_2$ points to their applicability in electrochemical analysis of OPC.

3.4. $\text{Co}^{\text{II}}@/\text{SiO}_2$ for Electrochemical Determination of OPC

The presentation of an electrochemical response of $\text{Co}^{\text{II}}@/\text{SiO}_2$ on OPC is worth preceding by the discussion of main mechanisms responsible for the response. Both oxidation and reduction of Co^{II} centers in $\text{Co}^{\text{II}}@/\text{SiO}_2$ are manifested in the CVs by the peaks with the peak currents dependent on concentration of the Co^{II} centers. The increased peak current of $\text{Co}^{\text{II}}/\text{Co}^{\text{III}}$ or $\text{Co}^{\text{II}}/\text{Co}^{\text{I}}$ transformations results from regeneration of Co^{II} centers due to rapid interaction of Co^{III} or Co^{I} with OPC. In turn,

the peak current can be significantly decreased in a case of unfavorable processes (the destruction of the catalytically active form or complex formation preventing a reestablishing of Co^{II} centers).

Both OPC (glyphosate and diethyl phosphite) are electrochemically inactive in the studied interval of potentials. Thus, the enhanced peak current at the oxidation and reduction potentials of w/o $\text{Co}^{\text{II}}@SiO_2$ under the increased concentrations of the OPC (Figure 8a,c) indicates that oxidized $\text{Co}^{\text{III}}@SiO_2$ or reduced $\text{Co}^{\text{I}}@SiO_2$ forms return to the initial form ($\text{Co}^{\text{II}}@SiO_2$) due to rapid redox reaction of Co^{III} or Co^{I} centers with the OPC. The concentration dependent increase in the peak current (Figure 8a,c) provides the electrochemical response on the OPC. The comparative analysis of the substrate-induced electrochemical response of $\text{Co}^{\text{II}}@SiO_2$ synthesized by w/o and Stöber procedures reveal a significant difference between them. The difference is the highest at the reduction potential, when Stöber $\text{Co}^{\text{II}}@SiO_2$ nanoparticles demonstrate a significant increase in the peak current under the growth of diethylphosphite concentration (Figure 8c), while glyphosate in the same conditions drops the peak current to zero (Figure 8d). It is worth assuming that the aforesaid fact correlates with the differences in the inner- and outer-sphere of Co^{II} ions within the silica spheres formed by the w/o and Stöber methods. Thus, the OPC-triggered electrochemical behavior of $\text{Co}^{\text{II}}@SiO_2$ is also greatly influenced by the method (Stöber or w/o) applied for their synthesis. Unfortunately, exact mechanisms responsible for the different electrochemical behavior of the hybrid nanoparticles in the presence of the OPC are not clear from the results. Additional studies lying beyond the present work scope are required for their clarification.

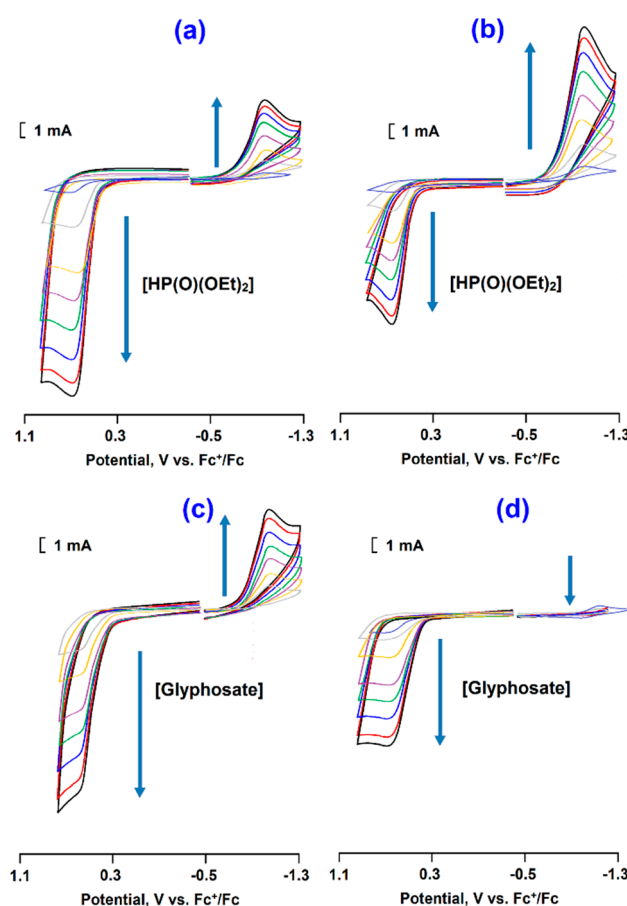


Figure 8. CVs for w/o $\text{Co}^{\text{II}}@SiO_2$ (a,c) and Stöber $\text{Co}^{\text{II}}@SiO_2$ (b,d) in the absence and in the presence of increasing quantities of HP(O)(OEt)_2 (a,b) and Glyphosate (c,d) (1.0, 2.5, 5.0, 10.0, 25.0, 50.0 $\text{mmol}\cdot\text{L}^{-1}$). WE: CPE, H_2O , $10^{-1} \text{ mol}\cdot\text{L}^{-1} \text{ Et}_4\text{NBF}_4$ Potentials vs. Ag/AgCl recalculated to Fc^+/Fc . Arrows indicate the direction of current changes.

Nevertheless, the presented results clearly demonstrate the applicability of the substrate-induced electrochemical response for quantitative analysis of the OPC. The increase in the peak current within anodic potentials range is greater than that within the cathodic range. For evaluation of a lower detection level (LOD), the peak current of $\text{Co}^{\text{II}}@\text{SiO}_2$ at different concentrations of the OPC was analyzed by differential impulse voltammetry technique (Figure 9 and Figure S6). The results (Figure 9a,b) indicate that even small amounts of the OPC ($0.1 \mu\text{mol}\cdot\text{L}^{-1}$) induce the detectable peak increase; thus, this concentration level can be considered as the LOD-value. Moreover, the inset in Figure 9 indicates the linear relationship between the response currents and HP(O)(OEt)_2 (red-black) and Glyphosate (gray-blue) concentrations in the range from 0.1 to $80 \mu\text{M}$ (with a correlation coefficient of 0.99). The slope of the linear dependencies is somewhat greater for w/o $\text{Co}^{\text{II}}@\text{SiO}_2$ versus Stöber $\text{Co}^{\text{II}}@\text{SiO}_2$, although the discrimination between glyphosate and diethylphosphite is rather poor for both types of $\text{Co}^{\text{II}}@\text{SiO}_2$. It is worth noting that glyphosate can be discriminated from diethylphosphite by the selective peak current increase in the cathodic range when the CPE was modified by Stöber $\text{Co}^{\text{II}}@\text{SiO}_2$.

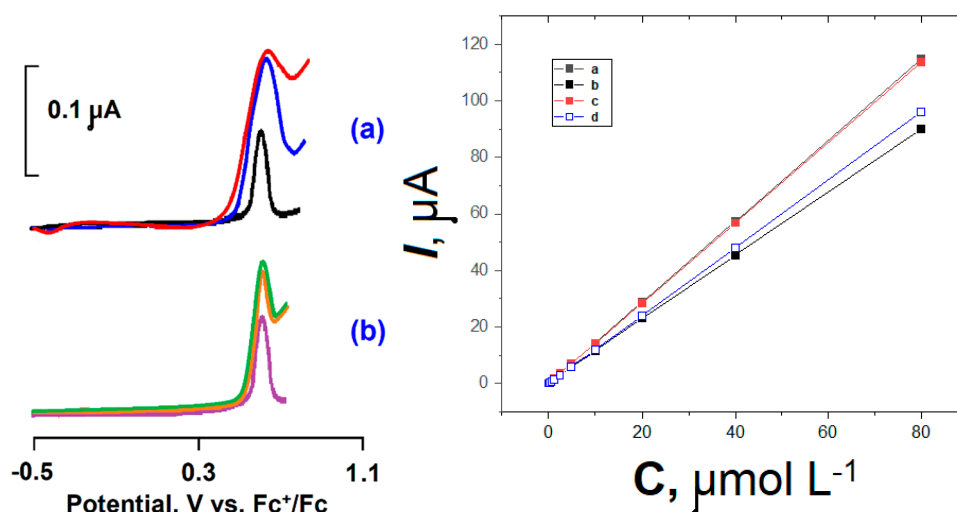


Figure 9. DPV voltammograms (on the left) of the $\text{Co}^{\text{II}}@\text{SiO}_2$ oxidation at CPE without and in the presence of increasing amounts of phosphorus compounds (at the first addition of OPC). (a): w/o $\text{Co}^{\text{II}}@\text{SiO}_2$ (black); w/o $\text{Co}^{\text{II}}@\text{SiO}_2 + 0.1 \mu\text{mol}\cdot\text{L}^{-1}$ HP(O)(OEt)_2 (blue); w/o $\text{Co}^{\text{II}}@\text{SiO}_2 + 0.1 \mu\text{mol}\cdot\text{L}^{-1}$ Glyphosate (red); (b): Stöber $\text{Co}^{\text{II}}@\text{SiO}_2$ (purple); Stöber $\text{Co}^{\text{II}}@\text{SiO}_2 + 0.1 \mu\text{mol}\cdot\text{L}^{-1}$ HP(O)(OEt)_2 (orange); Stöber $\text{Co}^{\text{II}}@\text{SiO}_2 + 0.1 \mu\text{mol}\cdot\text{L}^{-1}$ Glyphosate (Green); Potentials vs. Fc^+/Fc . H_2O , $10^{-1} \text{mol}\cdot\text{L}^{-1}$ Et_4NBF_4 . Corresponding plots of i_{cat} vs. OPC concentration (from 0.1 to $80 \mu\text{mol}\cdot\text{L}^{-1}$: 0.1, 0.2, 0.3, 0.6, 1.2, 2.4, 5.0, 10.0, 20.0, 40.0, $80.0 \mu\text{mol}\cdot\text{L}^{-1}$), the inset on the right: w/o $\text{Co}^{\text{II}}@\text{SiO}_2$ in the presence of Glyphosate (a, gray) and HP(O)(OEt)_2 (c, red); Stöber $\text{Co}^{\text{II}}@\text{SiO}_2$ in the presence of Glyphosate (d, blue) and HP(O)(OEt)_2 (b, black).

The estimated $\text{LOD} = 0.1 \mu\text{mol}\cdot\text{L}^{-1}$ is greater than the values reported for most sensitive sensing systems [21], but lower than the values reported for the colorimetric sensor [67]. The linearity of the peak current increase is manifested in a wider concentration range than the linearity range reported in [21] for electrochemical sensors based on $\text{Cu-BTC/g-C}_3\text{N}_4$ nanosheets ($\text{g-C}_3\text{N}_4$ = graphite phase nitrogenized carbon, BTC = benzene-1,3,5-tricarboxylic acid). Moreover, the present LOD-value is enough for evaluation of dose limit of glyphosate in a drinking water. Furthermore, the $\text{Co}^{\text{II}}@\text{SiO}_2$ based sensors have the characteristics of short detection time, high stability and easy operation, which is of great impact on potential applications in electrochemical OPC analysis.

4. Conclusions

In summary, analysis of size and content of silica nanoparticles doped by Co^{II} ions by means of water-in-oil microemulsion (w/o) or Stöber synthetic technique confirms the applicability of the both techniques for synthesis of the hybrid nanoparticles. Monitoring of the transformations of [Co(bpy)₃](BF₄)₂ used as the precursor for the hybrid nanoparticles through the UV-Vis spectral analysis during the synthesis highlights the decomposition of the precursor due to efficient coordination of the Co^{II} ions via Si-O⁻ groups exposed at the silica seeds. Thus, the use of either [Co(bpy)₃](BF₄)₂ or CoCl₂ as the precursors results in the nanoparticles with the same inner-sphere environment of the Co^{II} ions.

The analysis of the spectral properties in the wavelengths range of d-d transitions for the first time revealed preferable formation of tetrahedron Co^{II} chromophores versus the octahedral ones in the the Stöber nanoparticles, while the predominance of octahedral Co^{II} chromophores was observed in the w/o nanoparticles. Both IR and Raman spectra indicate one more difference between the w/o and Stöber methods. The nanoparticles synthesized by the former method are decorated by the TX-100-based corona arisen from the TX-100 molecules adsorbed at the surface of the nanoparticles synthesized by the w/o method.

PXRD analysis of the synthesized nanoparticles indicated their amorphous nature, although the nanocrystalline inclusions into amorphous phase was revealed for the Stöber nanoparticles, which differentiate them from the w/o ones. The SAXS data revealed the heterogeneity of both nanoparticles, which is manifested by the presence of core zones with greater electron density than the shell zone. The sizes of the core zone are below those evaluated from the TEM images. The deviation between the sizes obtained by the different techniques for the w/o nanoparticles is no more than 20%. This enables to assume that the shell zone derives from the porous silica surface decorated by the TX-100-based corona. Both significant (above 50%) deviation revealed between the size values obtained by TEM and SAXS and specific PXRD profiles indicate the nano-structuring of the Stöber nanoparticles.

The electrochemical behavior of the Co^{II} ions within the hybrid nanoparticles indicates the insignificant influence of the synthetic procedure at the first oxidation and reduction steps, while the second Co^I to Co⁰ reduction step is greatly influenced by the synthetic procedure. In particular, the reversible Co^I to Co⁰ reduction is facilitated within the w/o nanoparticles. The electrochemical behavior of the hybrid nanoparticles provides an efficient basis for electrochemical analysis of glyphosate and HP(O)(OEt)₂ with the lower detection limit at the level of 0.1 μmol·L⁻¹ with the linearity of the electrochemical response in the concentration range from 0.1 to 80 μmol·L⁻¹, short detection time, high stability, and easy operation. The sensing properties of the hybrid nanoparticles are also influenced by the synthetic method: the electrochemical response of the Stöber nanoparticles is able to discriminate glyphosate from HP(O)(OEt)₂, while the w/o nanoparticles are more efficient in the sensing of the both toxicants without discrimination between them.

Supplementary Materials: The following are available online at <http://www.mdpi.com/2079-4991/10/7/1338/s1>, Figure S1: UV-Vis spectra of supernatant diluted 300 times by ethanol after synthesis of w/o Co^{II}@SiO₂ (Co^{II}(bpy)₃ as precursor) (**blue**) and ethanol solutions of bpy (C = 5 × 10⁻⁵ mol·L⁻¹, **red**) and Triton X-100 (C = 0.9 g·L⁻¹, **black**), Figure S2: UV-Vis diffuse reflectance spectra of “empty” SiO₂, Figure S3: SAXS diffraction intensity profiles at 23 °C (in logarithmic scale) top to bottom: (**blue**) w/o Co^{II}@SiO₂ (CoCl₂ as precursor); (**red**) w/o Co^{II}@SiO₂ (Co^{II}(bpy)₃ as precursor); (**magenta**) Stöber Co^{II}@SiO₂ (CoCl₂ as precursor); (**green**) Stöber Co^{II}@SiO₂ (Co^{II}(bpy)₃ as precursor); (**dark**) “empty” Stöber SiO₂; (**dark blue**) “empty” w/o SiO₂. Scattering vector $s = 4\pi\sin\theta/\lambda$, Å⁻¹; $\lambda = 1.5418\text{Å}$ is the wavelength of the X-ray beam, Figure S4: X-ray scattering curves of w/o Co^{II}@SiO₂ in logarithmic (left) and double logarithmic (right) scale. Different colors of curves correspond to eight consistent experiments, Figure S5: The fitting of experimental SAXS curve (points – experimental data, curves – simulation) and calculated distance distribution function p(r) for: (a) w/o Co^{II}@SiO₂ (CoCl₂ as precursor); (b) w/o Co^{II}@SiO₂ (Co^{II}(bpy)₃ as precursor); (c) Stöber Co^{II}@SiO₂ (CoCl₂ as precursor); (d) Stöber Co^{II}@SiO₂ (Co^{II}(bpy)₃ as precursor); (e) “empty” Stöber SiO₂; (f) “empty” w/o SiO₂, Figure S6: DPV voltammograms for w/o Co^{II}@SiO₂ (a) and Stöber Co^{II}@SiO₂ (b) in the absence and in the presence of increasing quantities of Glyphosate (from 0.1 μmol·L⁻¹ to 80 μM: 0.1, 0.2, 0.3, 0.6, 1.2, 2.4, 5.0, 10.0, 20.0, 40.0, 80.0 μM). WE: CPE, H₂O, 10⁻¹ M Et₄NBF₄ Potentials vs. Ag/AgCl recalculated to Fc⁺/Fc. One-electron electron transfer during the oxidation and reduction of Co (II) is confirmed by

the coincidence of the oxidation currents of ferrocene under the same conditions at the same analyte concentration ($5 \times 10^{-3} \text{ mol} \cdot \text{L}^{-1}$).

Author Contributions: Conceptualization, A.M., Y.B., and A.G.; investigation, O.B., M.K., A.G., T.G., I.N., A.L., and K.K.; supervision, A.M. and O.S. All authors analyzed and discussed the data and wrote the manuscript. All authors have read and agreed to the published version of the manuscript.

Funding: The authors would like to thank the financial support from the government assignments for realization of scientific priority projects by the FRC Kazan Scientific Center of RAS.

Acknowledgments: The authors acknowledge the CSF-SAC FRC KSC RAS for providing necessary facilities to carry out all X-ray diffraction experiments and to register infrared and Raman spectra.

Conflicts of Interest: The authors declare no conflict of interest.

References

1. Antony, R.; Manickam, S.T.D.; Balakumar, S. Cu(II), Co(II) and Ni(II) Complexes Installed on Functionalized Silica Surface for Hydrogen Peroxide Assisted Cyclohexane Oxidation. *J. Inorg. Organomet. Polym. Mater.* **2017**, *27*, 418–426. [[CrossRef](#)]
2. Vashurin, A.; Marfin, Y.; Tarasyuk, I.; Kuzmin, I.; Znoyko, S.; Goncharenko, A.; Rummyantsev, E. Sulfonated octa-substituted Co(II) phthalocyanines immobilized on silica matrix as catalyst for Thiuram E synthesis. *Appl. Organomet. Chem.* **2018**, *32*, e4482. [[CrossRef](#)]
3. Faraji, A.R.; Mosazadeh, S.; Ashouri, F. Synthesis and characterization of cobalt-supported catalysts on modified magnetic nanoparticle: Green and highly efficient heterogeneous nanocatalyst for selective oxidation of ethylbenzene, cyclohexene and oximes with molecular oxygen. *J. Colloid Interface Sci.* **2017**, *506*, 10–26. [[CrossRef](#)] [[PubMed](#)]
4. Rajabi, F.; Luque, R.; Clark, J.H.; Karimi, B.; Macquarrie, D.J. A silica supported cobalt (II) Salen complex as efficient and reusable catalyst for the selective aerobic oxidation of ethyl benzene derivatives. *Catal. Commun.* **2011**, *12*, 510–513. [[CrossRef](#)]
5. Chen, L.; Li, B.-D.; Xu, Q.-X.; Liu, D.-B. A silica gel supported cobalt(II) Schiff base complex as efficient and recyclable heterogeneous catalyst for the selective aerobic oxidation of alkyl aromatics. *Chin. Chem. Lett.* **2013**, *24*, 849–852. [[CrossRef](#)]
6. Islam, S.M.; Ghosh, K.; Molla, R.A.; Roy, A.S.; Salam, N.; Iqbal, M.A. Synthesis of a reusable polymer anchored cobalt(II) complex for the aerobic oxidation of alkyl aromatics and unsaturated organic compounds. *J. Organomet. Chem.* **2014**, *774*, 61–69. [[CrossRef](#)]
7. Marfin, Y.S.; Vashurin, A.S.; Rummyantsev, E.V.; Puhovskaya, S.G. Sol-gel synthesis of highly effective catalyst based on cobalt tetrasulfophthalocyanine complex and silicon oxide. *J. Sol Gel Sci. Technol.* **2013**, *66*, 306–311. [[CrossRef](#)]
8. Ranaweera, S.A.; Rowe, M.D.; Walters, K.B.; Henry, W.P.; White, M.G.; Rodriguez, J.M. Synthesis, characterization and catalytic activity of a cobalt catalyst: Silica-supported, bis(1,5-diphenyl-1,3,5-pentanetrionato)dibobalt(II)[Co₂(dba)₂]. *Appl. Catal. A Gen.* **2017**, *529*, 108–117. [[CrossRef](#)]
9. Li-Juan, C.; Fu-Ming, M.; Guang-Xing, L. Co(II) Schiff base complexes on silica by sol-gel method as heterogeneous catalysts for oxidative carbonylation of aniline. *Catal. Commun.* **2009**, *10*, 981–985. [[CrossRef](#)]
10. Trujillano, R.; Lambert, J.-F.; Louis, C. Chemistry of Silica-Supported Cobalt Catalysts Prepared by Cation Adsorption. 2. Neoformation of Cobalt Phyllosilicate. *J. Phys. Chem. C* **2008**, *112*, 18551–18558. [[CrossRef](#)]
11. Yakubovich, T.N.; Ermokhina, N.I.; Bratushko, Y.I.; Zub, Y.L.; Chuiiko, A.A. Cobalt complex with 2,2'-bipyridyl immobilized on disperse silica surface in the reaction of p-hydroquinone oxidation. Comparison of the homogeneous and heterogeneous catalysis results. In *Dioxygen Activation and Homogeneous Catalytic Oxidation*; Simindi, L.I., Ed.; Elsevier Science Publishers, B.V.: Amsterdam, The Netherlands, 1991; pp. 179–188.
12. Rautiainen, A.; Lindblad, M.; Backman, L.B.; Puurunen, R.L. Preparation of silica-supported cobalt catalysts through chemisorption of cobalt(II) and cobalt(III) acetylacetonate. *Phys. Chem. Chem. Phys.* **2002**, *4*, 2466–2472. [[CrossRef](#)]
13. Yuanfa, Y.; Renxian, Z.; Shaofen, Z.; Qiaoling, L.; Xiaoming, Z. Silica-supported poly-γ-aminopropylsilane Ni²⁺, Cu²⁺, Co²⁺ complexes: Efficient catalysts for Heck vinylation reaction. *J. Mol. Catal. A Chem.* **2003**, *192*, 303–306. [[CrossRef](#)]

14. Khrizanforov, M.N.; Fedorenko, S.V.; Strekalova, S.O.; Kholin, K.V.; Mustafina, A.R.; Zhilkin, M.Y.; Khrizanforova, V.V.; Osin, Y.N.; Salnikov, V.V.; Gryaznova, T.V.; et al. A Ni(III) complex stabilized by silica nanoparticles as an efficient nanoheterogeneous catalyst for oxidative C–H fluoroalkylation. *Dalton Trans.* **2016**, *45*, 11976–11982. [[CrossRef](#)] [[PubMed](#)]
15. Khrizanforov, M.N.; Fedorenko, S.V.; Mustafina, A.R.; Khrizanforova, V.V.; Kholin, K.V.; Nizameev, I.R.; Gryaznova, T.V.; Grinenko, V.V.; Budnikova, Y.H. Nano-architecture of silica nanoparticles as a tool to tune both electrochemical and catalytic behavior of Ni^{II}@SiO₂. *RSC Adv.* **2019**, *9*, 22627–22635. [[CrossRef](#)]
16. Budnikova, Y.; Bochkova, O.; Khrizanforov, M.; Nizameev, I.; Kholin, K.; Gryaznova, T.; Laskin, A.; Dudkina, Y.; Strekalova, S.; Fedorenko, S.; et al. Selective C(sp²)-H Amination Catalyzed by High-Valent Cobalt(III)/(IV)-bpy Complex Immobilized on Silica Nanoparticles. *ChemCatChem* **2019**, *11*, 5615–5624. [[CrossRef](#)]
17. Ryabchuk, P.; Agostini, G.; Pohl, M.-M.; Lund, H.; Agapova, A.; Junge, H.; Junge, K.; Beller, M. Intermetallic nickel silicide nanocatalyst-A non-noble metal-based general hydrogenation catalyst. *Sci. Adv.* **2018**, *4*, eaat0761. [[CrossRef](#)]
18. Dudkina, Y.B.; Gryaznova, T.V.; Osin, Y.N.; Salnikov, V.V.; Davydov, N.A.; Fedorenko, S.V.; Mustafina, A.R.; Vicic, D.A.; Sinyashin, O.G.; Budnikova, Y.H. Nanoheterogeneous catalysis in electrochemically induced olefin perfluoroalkylation. *Dalton Trans.* **2015**, *44*, 8833–8838. [[CrossRef](#)]
19. Shabani-Nooshabadi, M.; Karimi-Maleh, H.; Tahernejad-Javazmi, F. Fabrication of an electroanalytical sensor for determination of deoxyepinephrine in the presence of uric acid using CuFe₂O₄ nanoparticle/ionic liquid amplified sensor. *J. Electrochem. Soc.* **2019**, *166*, H218. [[CrossRef](#)]
20. Liu, X. Electrochemical sensor for determination of parathion based on electropolymerization poly (safranin) film electrode. *Int. J. Electrochem.* **2011**, *2011*, 986494. [[CrossRef](#)]
21. Cao, Y.; Luona, W.; Chengyin, W.; Xiaoya, H.; Yunling, L.; Guoxiu, W. Sensitive detection of glyphosate based on a Cu-BTC MOF/g-C₃N₄ nanosheet photoelectrochemical sensor. *Electrochim. Acta* **2019**, *317*, 341–347. [[CrossRef](#)]
22. Shelkovnikov, V.V.; Novolokov, K.Y. Voltammetric sensor for determining malathion and diazinon. *Anal. Control* **2019**, *23*, 362–369. [[CrossRef](#)]
23. Tadayon, F.; Jahromi, M.N. A sensitive and selective electrochemical determination of Diazinon based on Au–Pd/rGO–MWCNTs composite: Analytical application in water, fruit and vegetable samples. *J. Iran. Chem. Soc.* **2020**, *17*, 847–857. [[CrossRef](#)]
24. Song, D.; Li, Y.; Lu, X.; Sun, M.; Liu, H.; Yu, G.; Gao, F. Palladium-copper nanowires-based biosensor for the ultrasensitive detection of organophosphate pesticides. *Anal. Chim. Acta* **2017**, *982*, 168–175. [[CrossRef](#)] [[PubMed](#)]
25. Zahirifar, F.; Rahimnejad, M.; Abdulkareem, R.A.; Najafpour, G. Determination of Diazinon in fruit samples using electrochemical sensor based on carbon nanotubes modified carbon paste electrode. *Biocatal. Agric. Biotechnol.* **2019**, *20*, 101245. [[CrossRef](#)]
26. Mahmoudi, E.; Fakhri, H.; Hajian, A.; Afkhami, A.; Bagheri, H. High-performance electrochemical enzyme sensor for organophosphate pesticide detection using modified metal-organic framework sensing platforms. *Bioelectrochemistry* **2019**, *130*, 107348. [[CrossRef](#)] [[PubMed](#)]
27. Sok, V.; Fragoso, A. Amperometric biosensor for glyphosate based on the inhibition of tyrosinase conjugated to carbon nano-onions in a chitosan matrix on a screen-printed electrode. *Microchim. Acta* **2019**, *186*, 569. [[CrossRef](#)]
28. Hua, Q.T.; Ruecha, N.; Hiruta, Y.; Citterio, D. Disposable electrochemical biosensor based on surface-modified screen-printed electrodes for organophosphorus pesticide analysis. *Anal. Methods* **2019**, *11*, 3439–3445. [[CrossRef](#)]
29. Hou, W.; Zhang, Q.; Dong, H.; Li, F.; Zhang, Y.; Guo, Y.; Sun, X. Acetylcholinesterase biosensor modified with ATO/OMC for detecting organophosphorus Pesticides. *New J. Chem.* **2019**, *43*, 946–952. [[CrossRef](#)]
30. Tefera, M.; Admassie, S.; Tessema, M.; Mehretie, S. Electrochemical sensor for determination of fenitrothion at multi-wall carbon nanotubes modified glassy carbon electrode. *Anal. Bioanal. Chem. Res.* **2015**, *2*, 139–150. [[CrossRef](#)]
31. Motaharian, A.; Motaharian, F.; Abnous, K.; Hosseini, M.R.M.; Hassanzadeh-Khayyat, M. Molecularly imprinted polymer nanoparticles-based electrochemical sensor for determination of diazinon pesticide in well water and apple fruit samples. *Anal. Bioanal. Chem.* **2016**, *408*, 6769–6779. [[CrossRef](#)]

32. Budnikov, G.K.; Evtuyugin, G.A.; Budnikova, Y.G.; Al'fonsov, V.A. Chemically modified electrodes with amperometric response in enantioselective analysis. *J. Anal. Chem.* **2008**, *63*, 2–12. [[CrossRef](#)]
33. Khanmohammadi, A.; Ghazizadeh, A.J.; Hashemi, P.; Afkhami, A.; Arduini, F.; Bagheri, H. An overview to electrochemical biosensors and sensors for the detection of environmental contaminants. *J. Iran. Chem. Soc.* **2020**, 1–19. [[CrossRef](#)]
34. Kokkinos, C.; Economou, A. Recent advances in voltammetric, amperometric and ion-selective (bio)sensors fabricated by microengineering manufacturing approaches. *Curr. Opin. Electrochem.* **2020**, *23*, 21–25. [[CrossRef](#)]
35. Wu, L.; Yan, H.; Wang, J.; Liu, G.; Xie, W. Tyrosinase Incorporated with Au-Pt@SiO₂ Nanospheres for Electrochemical Detection of Bisphenol, A. *J. Electrochem. Soc.* **2019**, *166*, B562. [[CrossRef](#)]
36. Jeerapan, I.; Poorahong, S. Review—Flexible and Stretchable Electrochemical Sensing Systems: Materials, Energy Sources, and Integrations. *J. Electrochem. Soc.* **2020**, *167*, 037573. [[CrossRef](#)]
37. Patel, B.R.; Noroozifar, M.; Kerman, K. Review—Nanocomposite-Based Sensors for Voltammetric Detection of Hazardous Phenolic Pollutants in Water. *J. Electrochem. Soc.* **2020**, *167*, 037568. [[CrossRef](#)]
38. Zhu, N.; Cai, H.; He, P.; Fang, Y. Tris(2,2'-bipyridyl)cobalt(III)-doped silica nanoparticle DNA probe for the electrochemical detection of DNA hybridization. *Anal. Chim. Acta* **2003**, *481*, 181–189. [[CrossRef](#)]
39. Zhang, D.; Wu, Z.; Xu, J.; Liang, J.; Li, J.; Yang, W. Tuning the Emission Properties of Ru(phen)₃²⁺ Doped Silica Nanoparticles by Changing the Addition Time of the Dye during the Stöber Process. *Langmuir* **2010**, *26*, 6657–6662. [[CrossRef](#)]
40. Lian, W.; Litherland, S.A.; Badrane, H.; Tan, W.; Wu, D.; Baker, H.V.; Gulig, P.A.; Lim, D.V.; Jin, S. Ultrasensitive detection of biomolecules with fluorescent dye-doped nanoparticles. *Anal. Biochem.* **2004**, *334*, 135–144. [[CrossRef](#)]
41. Ahkam, Q.M.; Khan, E.U.; Iqbal, J.; Murtaza, A.; Khan, M.T. Synthesis and characterization of cobalt-doped SiO₂ nanoparticles. *Phys. B Condens. Matter* **2019**, *572*, 161–167. [[CrossRef](#)]
42. Bai, S.H.; Ogbourne, S.M. Glyphosate: Environmental contamination, toxicity and potential risks to human health via food contamination. *Env. Sci. Pollut. Res.* **2016**, *23*, 18988–19001. [[CrossRef](#)]
43. Khrizanforov, M.; Gryaznova, T.; Sinyashin, O.; Budnikova, Y. Aromatic perfluoroalkylation with metal complexes in electrocatalytic conditions. *J. Organomet. Chem.* **2012**, *718*, 101–104. [[CrossRef](#)]
44. Mustafina, A.R.; Fedorenko, S.V.; Konovalova, O.D.; Menshikova, A.Y.; Shevchenko, N.N.; Soloveva, S.E.; Konovalov, A.I.; Antipin, I.S. Novel Highly Charged Silica-Coated Tb(III) Nanoparticles with Fluorescent Properties Sensitive to Ion Exchange and Energy Transfer Processes in Aqueous Dispersions. *Langmuir* **2009**, *25*, 3146–3151. [[CrossRef](#)]
45. Khrizanforov, M.N.; Arkhipova, D.M.; Shekurov, R.P.; Gerasimova, T.P.; Ermolaev, V.V.; Islamov, D.R.; Miluykov, V.A.; Kataeva, O.N.; Khrizanforova, V.V.; Sinyashin, O.G.; et al. Novel paste electrodes based on phosphonium salt room temperature ionic liquids for studying the redox properties of insoluble compounds. *J. Solid State Electrochem.* **2015**, *19*, 2883–2890. [[CrossRef](#)]
46. *DIFFRAC Plus Evaluation package EVA*; Version 11; User's Manual; Bruker AXS: Karlsruhe, Germany, 2005.
47. *Small Angle X-ray Scattering*; Version 4.0; Software Reference Manual, M86-E00005-0600; Bruker AXS Inc.: Madison, WI, USA, 2000.
48. Konarev, P.V.; Volkov, V.V.; Sokolova, A.V.; Koch, M.H.J.; Svergun, D.I. PRIMUS: A Windows PC-based system for small-angle scattering data analysis. *J. Appl. Cryst.* **2003**, *36*, 1277–1282. [[CrossRef](#)]
49. Arriagada, F.J.; Osseo-Asare, K. Controlled hydrolysis of tetraethoxysilane in a nonionic water-in-oil microemulsion: A statistical model of silica nucleation. *Colloids Surf. A Physicochem. Eng. Asp.* **1999**, *154*, 311–326. [[CrossRef](#)]
50. Liver, E. *Elektronnaya Spektroskopiya Neorganicheskikh Soedineniy (Electron Spectroscopy of Inorganic Compounds)*, 2nd ed.; Mir: Moscow, Russia, 1987.
51. Alexandru, M.-G.; Velickovic, M.; Hrubaru, K.M.-M.; Draghici, C. Two complexes of Co(II) and Pd(II) formed in reaction with a mono-T.C. oxazoline derivative. Spectroscopic characterization and cytotoxic evaluation. *J. Mol. Struct.* **2013**, *1041*, 55–60. [[CrossRef](#)]
52. Verberckmoes, A.A.; Weckhuysen, B.M.; Schoonheydt, R.A. Spectroscopy and coordination chemistry of cobalt in molecular sieves. *Microporous Mesoporous Mater.* **1998**, *22*, 165–178. [[CrossRef](#)]

53. Gerasimova, T.; Shekurov, R.; Gilmanova, L.; Laskin, A.; Katsyuba, S.; Kovalenko, V.; Khrizanforov, M.; Milyukov, V.; Sinyashin, O. IR and UV study of reversible water-induced structural transformations of poly(manganese 1,10-ferrocenediyl-bis(Hphosphinate)) and poly(cobalt 1,10-ferrocenediyl-bis(H-phosphinate)). *J. Mol. Struct.* **2018**, *1166*, 237–242. [[CrossRef](#)]
54. Shekurov, R.; Khrizanforova, V.; Gilmanova, L.; Khrizanforov, M.; Miluykov, V.; Kataeva, O.; Yamaleeva, Z.; Burganov, T.; Gerasimova, T.; Khamatgalimov, A.; et al. Zn and Co redox active coordination polymers as efficient electrocatalysts. *Dalton Trans.* **2019**, *48*, 3601–3609. [[CrossRef](#)]
55. Yousef, T.A.; El-Reash, G.M.A.; El-Gammal, O.A.; Bedier, R.A. Co(II), Cu(II), Cd(II), Fe(III) and U(VI) complexes containing a NSNO donor ligand: Synthesis, characterization, optical band gap, in vitro antimicrobial and DNA cleavage studies. *J. Mol. Struct.* **2012**, *1029*, 149–160. [[CrossRef](#)]
56. Kang, W.; Spanjers, C.S.; Rioux, R.M.; Hoefelmeyer, J.D. Synthesis of brookite TiO₂ nanorods with isolated Co(II) surface sites and photocatalytic degradation of 5,8-dihydroxy-1,4-naphthoquinone dye. *J. Mater. Chem. A* **2013**, *1*, 7717–7728. [[CrossRef](#)]
57. Islam, S.; Bakhtiar, H.; Aziz, M.S.B.A.; Duralima, M.B.; Riaz, S.; Naseemb, S.; Abdulla, M.B.; Osman, S.S. CR incorporation in mesoporous silica matrix for fiber optic pH sensing. *Sens. Actuators A Phys.* **2018**, *280*, 429–436. [[CrossRef](#)]
58. Islam, S.; Bakhtiar, H.; Naseem, S.; Aziz, M.S.B.A.; Biden, N.; Riaz, S.; Ali, J. Surface functionality and optical properties impact of phenol red dye on mesoporous silica matrix for fiber optic pH sensing. *Sens. Actuators A Phys.* **2018**, *276*, 267–277. [[CrossRef](#)]
59. Chen, C.; Xu, J.; Zhang, Q.; Ma, H.; Miao, H.; Zhou, L. Direct synthesis of bifunctionalized hexagonal mesoporous silicas and its catalytic performance for aerobic oxidation of cyclohexane. *J. Phys. Chem. C* **2009**, *113*, 2855–2860. [[CrossRef](#)]
60. Fouad, O.A.; Makhlof, S.A.; Ali, G.A.M.; El-Sayed, A.Y. Cobalt/silica nanocomposite via thermal calcination-reduction of gel precursors. *Mater. Chem. Phys.* **2011**, *128*, 70–76. [[CrossRef](#)]
61. Genovese, D.; Rampazzo, E.; Bonacchi, S.; Montalti, M.; Zaccheroni, N.; Prodi, L. Energy transfer processes in dye-doped nanostructures yield cooperative and versatile fluorescent probes. *Nanoscale* **2014**, *6*, 3022–3036. [[CrossRef](#)] [[PubMed](#)]
62. Koirala, R.; Safonova, O.V.; Pratsinis, S.E.; Baiker, A. Effect of cobalt loading on structure and catalytic behavior of CoO_x/SiO₂ in CO₂-assisted dehydrogenation of ethane. *Appl. Catal. A* **2018**, *552*, 77–85. [[CrossRef](#)]
63. Okamoto, Y.; Nagata, K.; Adachi, T.; Imanaka, T.; Inamura, K.; Takyu, T. Preparation and Characterization of Highly Dispersed Cobalt Oxide and Sulfide Catalysts Supported on SiO₂. *J. Phys. Chem.* **1991**, *95*, 310–319. [[CrossRef](#)]
64. Masalov, V.M.; Kudrenko, E.A.; Grigoryeva, N.A.; Ezdakova, K.V.; Roddatis, V.V.; Sukhinina, N.S.; Arefev, M.V.; Mistonov, A.A.; Grigoriev, S.V.; Emelchenko, G.A. Direct observation of the shell-like structure of SiO₂ particles synthesized by the multistage Stober method. *Nano Brief Rep. Rev.* **2013**, *8*, 1350036. [[CrossRef](#)]
65. Fouilloux, S.; Désert, A.; Taché, O.; Spalla, O.; Daillant, J.; Thill, A. SAXS exploration of the synthesis of ultra monodisperse silica nanoparticles and quantitative nucleation growth modeling. *J. Colloid Interface Sci.* **2010**, *346*, 79–86. [[CrossRef](#)] [[PubMed](#)]
66. Fouilloux, S.; Daillant, J.; Thill, A. Single step synthesis of 5–30 nm monodisperse silica nanoparticles: Important experimental parameters and modeling. *Colloids Surf. A Physicochem. Eng. Asp.* **2012**, *393*, 122–127. [[CrossRef](#)]
67. De Almeida, L.K.S.; Chigome, S.; Torto, N.; Frost, C.L.; Pletschke, B.I. A novel colorimetric sensor strip for the detection of glyphosate in water. *Sens. Actuators B Chem.* **2015**, *206*, 357–363. [[CrossRef](#)]

